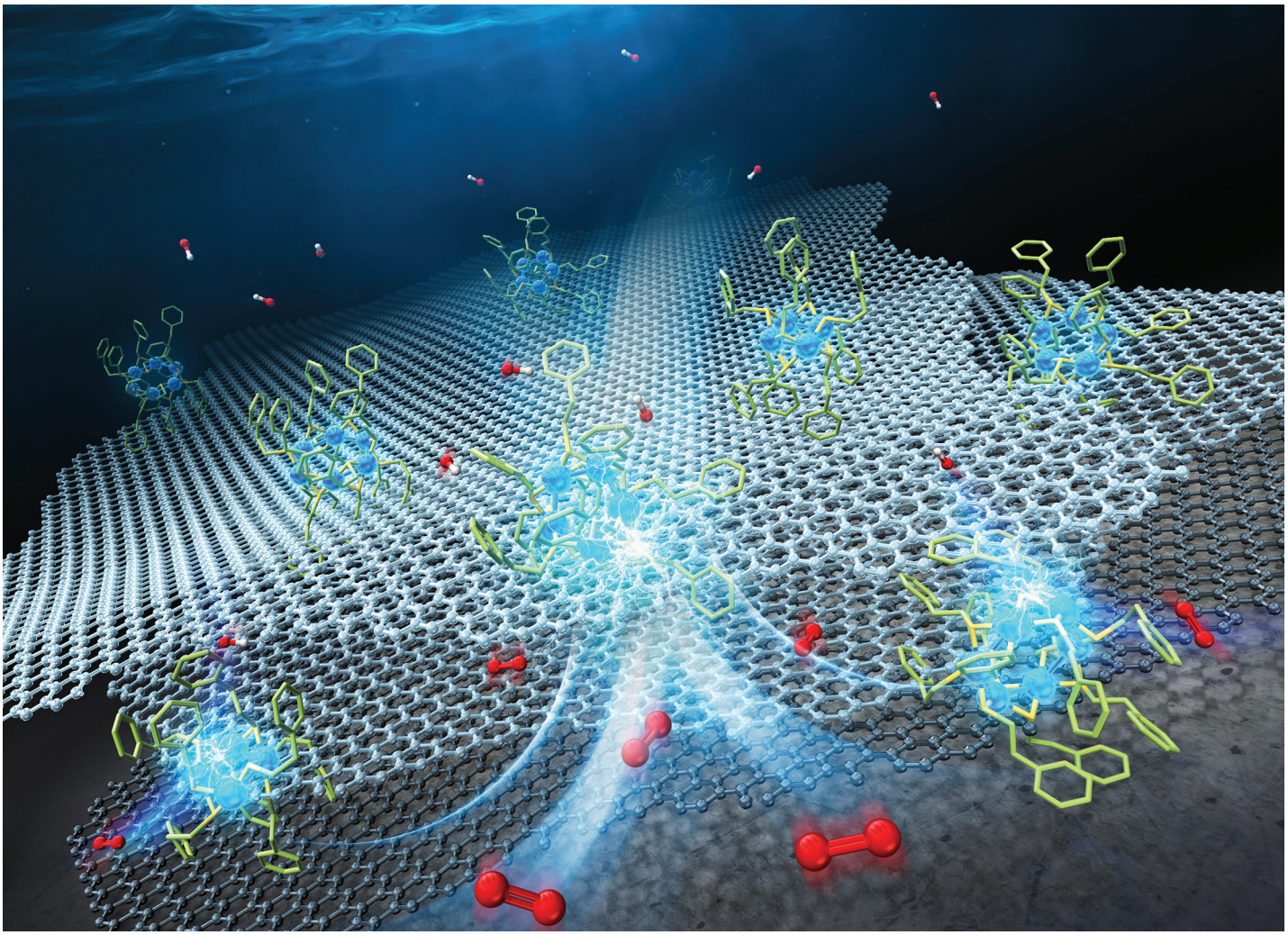

Showcasing research from Prof. Yuichi Negishi's laboratory, Tokyo University of Science, Japan.

Improved activity for the oxygen evolution reaction using a tiara-like thiolate-protected nickel nanocluster

Facilitating the oxygen evolution reaction (OER, the reaction at the anode) will increase the efficiency of electrochemical water-splitting and carbon dioxide reduction. Nickel (Ni) compounds are excellent OER catalysts under basic conditions. This study determined the geometric/electronic structure of tiara-like nickel (Ni) nanoclusters [$Ni_n(PET)_{2n}$; n = 4, 5, 6, where PET refers to phenylethanethiolate]. In addition, combined electrochemical measurements and X-ray absorption fine structure measurements revealed that $Ni_5(SR)_{10}$ easily forms an OER intermediate and therefore exhibits a high specific activity.

As featured in:

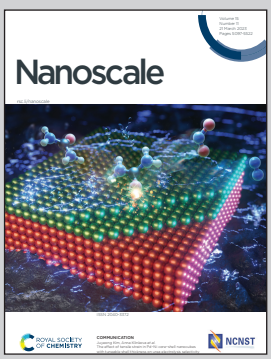

See Tokuhisa Kawawaki, Yuichi Negishi *et al.*, *Nanoscale*, 2023, **15**, 5201.

ROYAL SOCIETY OF CHEMISTRY

rsc.li/nanoscale

Registered charity number: 207890

Nanoscale

ROYAL SOCIETY OF CHEMISTRY

PAPER

View Article Online
View Journal | View Issue

Open Access Article. Published on 07 February 2023. Downloaded on 4/30/2026 8:17:38 PM.
This article is licensed under a Creative Commons Attribution-NonCommercial 3.0 Unported Licence.

Check for updates

Cite this: *Nanoscale*, 2023, **15**, 5201

Improved activity for the oxygen evolution reaction using a tiara-like thiolate-protected nickel nanocluster†

Sota Funaki,[a] Tokuhisa Kawawaki,[a,b]* Tomoshige Okada,[a] Kana Takemae,[a] Sakiat Hossain,[b] Yoshiki Niihori,[b] Takumi Naito,[c] Makito Takagi,[c] Tomomi Shimazaki,[c] Soichi Kikkawa,[d] Seiji Yamazoe,[d] Masanori Tachikawa[c] and Yuichi Negishi[a,b]*

Received 12th December 2022,
Accepted 7th February 2023

DOI: 10.1039/d2nr06952k

rsc.li/nanoscale

Practical electrochemical water splitting and carbon-dioxide reduction are desirable for a sustainable energy society. In particular, facilitating the oxygen evolution reaction (OER, the reaction at the anode) will increase the efficiency of these reactions. Nickel (Ni) compounds are excellent OER catalysts under basic conditions, and atomically precise Ni clusters have been actively studied to understand their complex reaction mechanisms. In this study, we evaluated the geometric/electronic structure of tiara-like metal nanoclusters [$Ni_n(PET)_{2n}$; n = 4, 5, 6, where PET refers to phenylethanethiolate] with the same SR ligand. The geometric structure of $Ni_5(SR)_{10}$ was determined for the first time using single-crystal X-ray diffraction. Additionally, combined electrochemical measurements and X-ray absorption fine structure measurements revealed that $Ni_5(SR)_{10}$ easily forms an OER intermediate and therefore exhibits a high specific activity.

Introduction

Polynuclear metal complexes, termed metal nanoclusters (NCs), exhibit physicochemical properties that differ from those of bulk metals composed of the same metal elements. These metal NCs can be synthesized as stable compounds using thiolate (SR),[1–8] which plays a role in preventing the oxidation of metal atoms from air. Furthermore, such metal NCs have attracted much attention as highly functional new materials in catalysis, bioimaging, and sensing.[9–13] In particular, tiara-like metal NCs (TNCs) are cyclic compounds containing metals. TNCs composed of group 10 transition metals can be synthesized easily with atomic precision under air using SR ligands.[14,15] Furthermore, the synthesized TNCs can be separated by thin-layer chromatography (TLC), gel permeation chromatography, or high-performance liquid chromatography to obtain TNCs with atomic precision.[16–18] Tiara-like nickel (Ni) NCs ($Ni_n(SR)_{2n}$) including various numbers of metal atoms have also been synthesized with several SR ligands[19–34] and their applications have been studied, including hydrogenation of nitrophenol[35] and nitrile,[36] oxidation of ascorbic acid,[37] hydrogen evolution from water using a photocatalyst[38] or an electrocatalyst,[39] and photocatalytic methane oxidation.[40]

Meanwhile, in recent years, researchers have focused on achieving practical use of electrochemical water splitting and carbon-dioxide reduction for the realization of a sustainable energy society. However, the efficient use of the oxygen evolution reaction (OER, an anodic reaction occurring at the counter electrode in both reactions) is particularly important for further enhancement of the functionality of these reaction systems. The base metal Ni is an excellent OER catalyst under basic conditions, and $Ni_n(SR)_{2n}$ exhibits a high OER activity.[41–43] Thus, the use of metal NCs with unambiguous structures as catalysts is expected to help researchers understand the correlation between electrocatalytic activity and the geometric structure of the catalysts, and thereby elucidate the mechanism of electrocatalytic activity.[44–48] However, few reports have compared the structure and OER activity of $Ni_n(SR)_{2n}$ (n = 4, 5, 6) with the same SR ligand, and the corre-

[a]Department of Applied Chemistry, Faculty of Science, Tokyo University of Science, 1-3 Kagurazaka, Shinjuku-ku, Tokyo 162-8601, Japan.
E-mail: kawawaki@rs.tus.ac.jp, negishi@rs.tus.ac.jp; Fax: +81-3-5261-4631; Tel: +81-3-5228-9145
[b]Research Institute for Science and Technology, Tokyo University of Science, 1-3 Kagurazaka, Shinjuku-ku, Tokyo 162-8601, Japan
[c]Graduate School of NanoBioScience, Yokohama City University, 22-2 Seto, Kanazawa-ku, Yokohama 236-0027, Japan
[d]Department of Chemistry, Graduate School of Science, Tokyo Metropolitan University, 1-1 Minami-Osawa, Hachioji-shi, Tokyo 192-0397, Japan

† Electronic supplementary information (ESI) available: Experimental; characterization; crystal data; peak assignments of FT-IR spectroscopy; additional UV-vis, XPS, FT-IR, XANES, and EXAFS spectra; TEM images; and electrocatalytic activity. CCDC 2212626. For ESI and crystallographic data in CIF or other electronic format see DOI: https://doi.org/10.1039/d2nr06952k

Open Access Article. Published on 07 February 2023. Downloaded on 4/30/2026 8:17:38 PM.
This article is licensed under a Creative Commons Attribution-NonCommercial 3.0 Unported Licence.

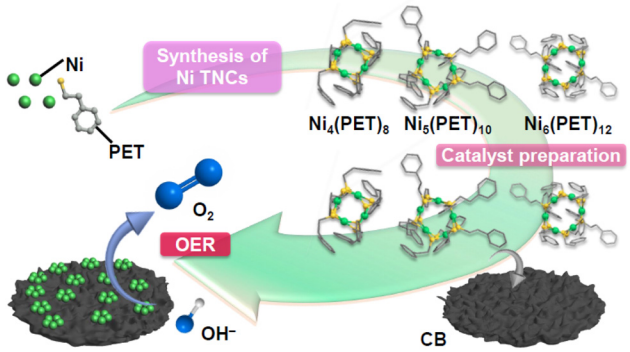

Fig. 1 Schematic of the purpose of this study. TNC: tiara-like metal nanocluster. PET: 2-phenylethanethiolate. CB: carbon black. OER: oxygen evolution reaction.

lation between the structure and activity is still unclear in many cases.[41–43] Therefore, it is desirable to elucidate the geometric structure and its correlation with the OER activity using the same type of SR ligand for $Ni_n(SR)_{2n}$ (n = 4, 5, 6) (Fig. 1).

In this study, we successfully determined the geometric structure of $Ni_5(PET)_{10}$ (PET = 2-phenylethanethiolate) for the first time by single-crystal X-ray diffraction (SC-XRD). Using the obtained $Ni_n(PET)_{2n}$ (n = 4, 5, 6), we also prepared $Ni_n(PET)_{2n}$/carbon black (CB) (n = 4, 5, 6) catalysts with a higher OER activity than general Ni oxide (NiO) nanoparticle (NP) catalysts. Furthermore, among the $Ni_n(PET)_{2n}$/CB (n = 4, 5, 6), $Ni_5(PET)_{10}$/CB exhibited particularly high OER activity compared with $Ni_4(PET)_8$/CB and $Ni_6(PET)_{12}$/CB because of easy formation of an OER intermediate.

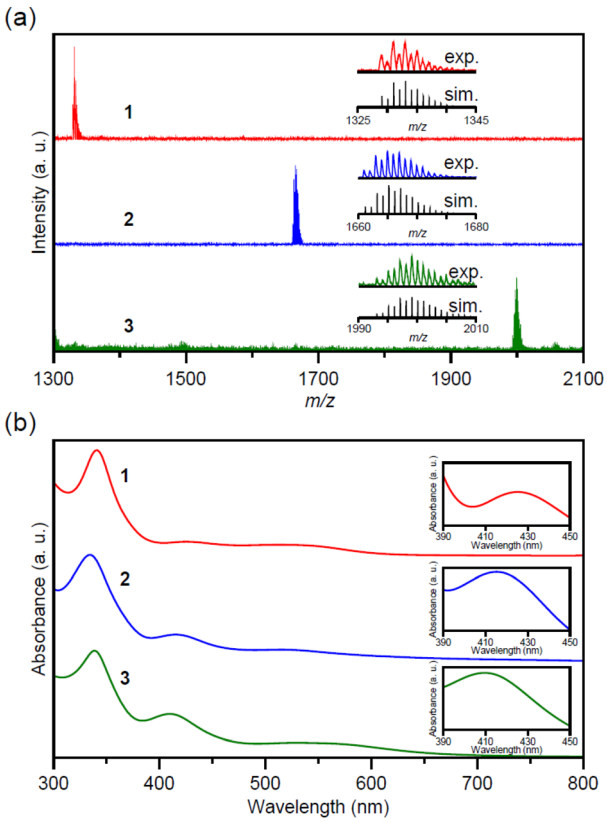

Fig. 2 (a) Positive-ion MALDI mass spectra of **1–3**. Insets: comparison of the isotope pattern between the experimental spectra (exp; red, **1**; blue, **2**; green, **3**) and the simulated spectra (sim; black). (b) UV-Vis absorption spectra of **1–3**. Insets: comparison of peak maxima at ~410 nm.

Results and discussion

Characterization of $Ni_n(PET)_{2n}$ (n = 4, 5, 6)

The matrix-assisted laser desorption/ionization (MALDI) mass spectra of the obtained products (**1–3**) are shown in Fig. 2a and S1.† Compounds **1–3** exhibited peaks centered at m/z = 1332, 1664, and 1998, respectively, in the positive ionization mode. The interval of the isotope pattern was m/z = 1, indicating that the products were monovalent. The peak positions of **1–3** are in good agreement with $[Ni_n(PET)_{2n} + H]^+$ (n = 4, 5, 6), respectively.[49] The ultraviolet–visible (UV-Vis) absorption spectra of **1–3** indicate similar shapes to the previously reported spectra of $Ni_n(PET)_{2n}$ (n = 4, 5, 6) (Fig. 2b). In the Fourier-transform infrared (FT-IR) spectra, the peaks were attributable to phenyl and ethylene groups in PET (Fig. S2 and Table S1†). On the basis of these results, we determined **1–3** as $[Ni_n(PET)_{2n}]^0$ (n = 4, 5, 6), respectively.

Fig. S3 and S4† show the results of X-ray absorption fine structure (XAFS) measurements of **1–3**. In the Ni K-edge X-ray absorption near-edge structure (XANES) spectra of **1–3** (Fig. S3†), we observed a broad pre-edge peak originating from the transition of the tetracoordinated divalent Ni ion (Ni^{2+}) from the 1s to the 3d orbital at ~8331 eV similar to NiO and $Ni(OH)_2$. There were almost no differences in the position of this peak between **1** and **3**, indicating that the Ni 3d orbitals in **1–3** were similar. In addition, we observed a peak at ~8336 eV in the spectra of **1–3**. This peak is attributable to the transition from 1s to 4p of Ni^{2+} and the charge transfer (CT) transition to the ligands, indicating the presence of a strong covalent Ni–S bond in **1–3**.[50,51] Fig. S4† shows the Ni K-edge Fourier-transform extended XAFS (FT-EXAFS) spectra of **1–3**. We did not observe peaks derived from Ni–O bonds (~1.8 Å), Ni–Ni bonds (~2.1 Å), or Ni–O–Ni bonds (~2.6 Å); only a peak (1.9 Å) derived from Ni–S bonds was observed.[51–55] These results indicate that Ni was directly bonded to the S in PET as the ligand in **1–3**.

The UV-Vis absorption spectra of **1–3** in Fig. 2b show the characteristic absorption peaks from ~340 to ~410 nm, and these exhibited overall similar shapes. This indicates that **1–3** had similar electronic structures overall. Additionally, the absorption peak at ~410 nm shifted to shorter wavelengths and the absorption intensity increased, with an increasing number of Ni atoms. We performed density functional theory (DFT) calculations of $[Ni_6(PET)_{12}]^0$ (**3**) to elucidate these features. First, we calculated the optimized structures (Fig. S5†) in tetrahydrofuran (THF) (**3′**) and in a vacuum (**3″**) of

 This journal is © The Royal Society of Chemistry 2023

Open Access Article. Published on 07 February 2023. Downloaded on 4/30/2026 8:17:38 PM.
This article is licensed under a Creative Commons Attribution-NonCommercial 3.0 Unported Licence.

$[Ni_6(PET)_{12}]^0$ and then calculated the corresponding optical absorption spectra (Fig. S6†). The results revealed the following: (1) ~410 nm peak in the UV-Vis spectrum of **3** is mainly due to d–d transitions between Ni atoms and (2) ~340 nm peak is mainly caused by CT transitions from the phenyl group to Ni and the S in PET. Previous studies by other groups have also attributed the absorption peak at ~340 nm to the CT transition from the PET-derived S 3p π orbital to the Ni 3d orbital;[41,49] our calculations are consistent with these previous reports. On the basis of the results of these DFT calculations, we interpreted the change in the absorption peak at ~410 nm observed in Fig. 2b with the differences in the number of Ni atoms to be due to the differences in the distance between the Ni and Ni of **1–3** described in a subsequent paragraph.

Regarding the geometric structure of $[Ni_n(PET)_{2n}]^0$ (n = 4, 5, 6), a previous study has revealed the geometric structures of $[Ni_4(PET)_8]^0$ (**1**) and $[Ni_6(PET)_{12}]^0$ (**3**) by SC-XRD (Fig. 3a, b and S7†).[42] However, the geometric structure of $[Ni_5(PET)_{10}]^0$ has only been predicted by theoretical calculations. In this study, we determined the geometric structure of $[Ni_5(PET)_{10}]^0$ (**2**) by SC-XRD for the first time (Fig. 3a, b and Table S2†). The result revealed that $[Ni_5(PET)_{10}]^0$ consisted of a ring with five Ni atoms in the plane and five S atoms bridged above and below the plane, in total ten S atoms, almost as predicted by theoretical calculations.

Next, we compared the obtained geometric structures of $[Ni_n(PET)_{2n}]^0$ (n = 4, 5, 6) (Fig. 4 and S8; Tables S3 and S4†). The average bond length of the Ni–S bonds and the average angles of the S–Ni–S bonds in **1–3** were ~2.20 Å and ~98°, respectively, indicating no differences in terms of the number of constituent Ni atoms. Regarding the average Ni–Ni–Ni angle, these are ideal angles in regular polygons (90.0°, 108.0°, and 120.0°). However, the average length of the Ni–Ni distance

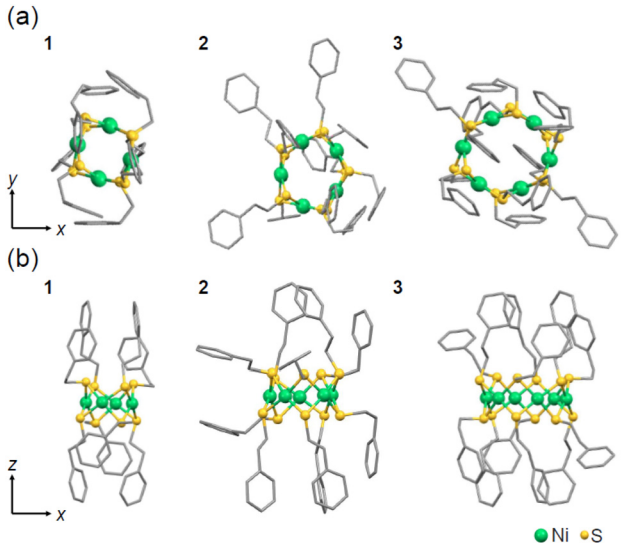

Fig. 3 Geometric structure of **1–3** determined by SC-XRD from (a) the top view and (b) the side view. Hydrogen atoms and solvents are omitted for clarity. Ni: light green, S: yellow, and carbon: gray. The geometric structures of **1** and **3** were obtained from ref. 42.

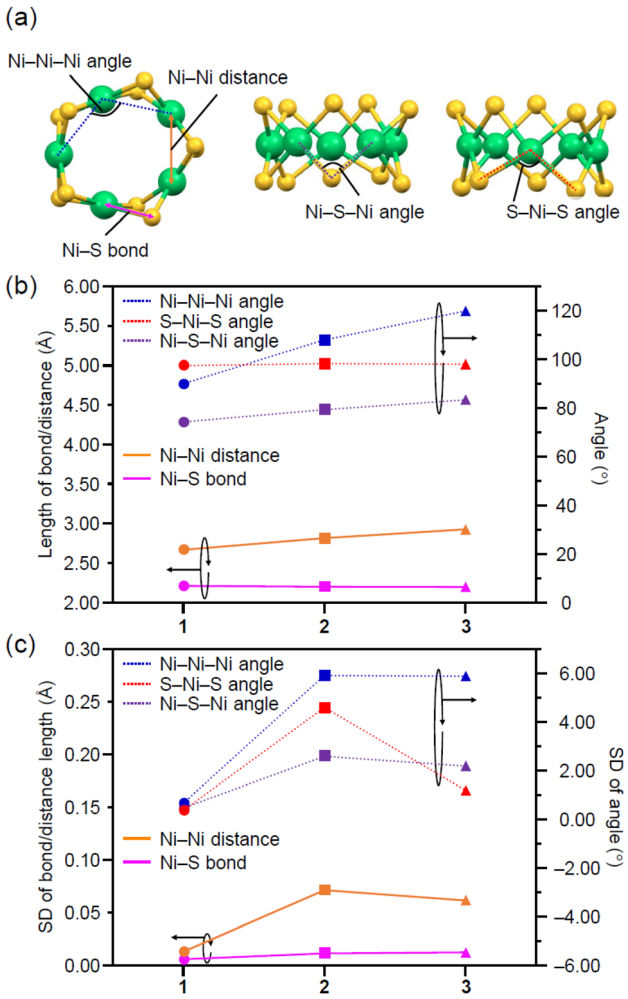

Fig. 4 (a) Relevant geometric parameters for the structure of **2**. (b) Averages and (c) standard deviations of Ni–Ni–Ni, S–Ni–S, and Ni–S–Ni angles (°)and lengths of the Ni–Ni distance and the Ni–S bond (Å). SD: standard deviation. Relevant geometric parameters used for the analysis of structures **1–3** are shown in Fig. S8(A).† In (c), the SD represents the disorder of each interatomic distance and angle, and a larger SD means a more distorted structure of compounds.

(from 2.67 Å to 2.93 Å) and the average Ni–S–Ni angle (from 74.3° to 83.5°) increased as the number of constituent Ni atoms increased. These results indicate that in **1–3**, the Ni–S–Ni angle extended in the horizontal direction of the ring structure with an increase in the number of constituent Ni atoms while maintaining the Ni–S bond length (Fig. 4a, b and S8†). These features are overall in good agreement with those reported for $Ni_n(SR)_{2n}$ (n = 4–12) with different ligands.[34]

Regarding the average angles for Ni–Ni–Ni, S–Ni–S, and Ni–S–Ni bonds in these geometric structures, **2** had the largest standard deviation (SD). This indicates that **2** exhibits the most distorted geometric structure among **1–3**. The direction of PET alternates between the vertical (V site) and horizontal (H site) directions against the ring structure to avoid steric repulsion between PETs (Fig. S9†). In the case of **1** and **3**, which form even-numbered polygons, this alternation between

Open Access Article. Published on 07 February 2023. Downloaded on 4/30/2026 8:17:38 PM.
This article is licensed under a Creative Commons Attribution-NonCommercial 3.0 Unported Licence.

PETs is possible. However, in the case of **2**, which forms odd-numbered polygons, such a perfect alternation is not possible.[56] We can interpret that the distortion of the structure was larger in **2** than in **1** and **3** due to this imperfect alternation. Regarding $M_n(SR)_{2n}$ (M = Ni; palladium, Pd; platinum, Pt), many studies have reported the synthesis of $M_n(SR)_{2n}$ with an even number of metal atoms.[17–21,23,24,27,28,30,32–34] This is assumed to be largely related to their high stability caused by a perfect alternation. In addition, the distortion of the structure in **2** is larger than that in $Ni_5(SCH_2CH_3)_{10}$ and $Ni_5(SCH_2SiMe_3)_{10}$.[25,26] It can be considered that since PET exhibits a bulkier geometric structure than SCH_2SiMe_3 and SCH_2CH_3, a larger strain occurs in **2** than in $Ni_5(SCH_2SiMe_3)_{10}$ and $Ni_5(SCH_2CH_3)_{10}$ (Fig. S10, Tables S5 and S6†).

We also examined the stability of **1–3** against deterioration in solution by tracking the change in the optical absorption of **1–3** dissolved in THF over time. We observed no substantial differences in the stability of **1–3** (Fig. S11†). As shown in Fig. S7,† there were π–π and C–H···π interactions between phenyl groups at the surface of **1–3**. We assume that these ligand interactions suppress the dissociation of **1–3**,[57] leading to the fact that **2** also exhibits the same stability as **1** and **3**. Thus, when we use PET as the ligand, **2** (an odd number of metal atoms) could also be stably isolated.

Characterization of $Ni_n(PET)_{2n}$(n = 4, 5, 6)/CB and NiO-IM/CB

We prepared $Ni_n(PET)_{2n}$/CB (n = 4, 5, 6) catalysts using **1–3** (see the Experimental section). In addition, a NiO NP catalyst (NiO-IM/CB) (IM; impregnation) was prepared for comparison. The XAFS spectra of $Ni_n(PET)_{2n}$/CB (n = 4, 5, 6) (Fig. S12–S15†) implied that there were no substantial changes in the geometric/electronic structures of $Ni_n(PET)_{2n}$ (n = 4, 5, 6) before and after adsorption of **1–3** on CB. Fig. 5 shows transmission electron microscopy (TEM) images (Fig. S16†), high-angle annular dark-field scanning TEM (HAADF-STEM) images, and energy-dispersive spectroscopy (EDS) elemental mapping (Fig. S17 and S18†) of $Ni_n(PET)_{2n}$/CB (n = 4, 5, 6). The average particle sizes of $Ni_n(PET)_{2n}$ (n = 4, 5, 6) on CB were *ca.* 0.6 ± 0.1, 0.6 ± 0.1, and 0.7 ± 0.1 nm, respectively. HAADF-STEM images and EDS elemental mapping confirmed that $Ni_n(PET)_{2n}$ (n = 4, 5, 6) were adsorbed monodispersely on CB (Fig. 5 and S17†). These results indicate that $Ni_n(PET)_{2n}$ (n = 4, 5, 6) were loaded uniformly on CB without aggregation in this study. Experiments with different loading weights of $Ni_n(PET)_{2n}$ (Fig. S16 and S19†) revealed that at least up to 5 wt% of Ni could be loaded onto CB without aggregation of $Ni_n(PET)_{2n}$ (n = 4, 5, 6).

OER activity of $Ni_n(PET)_{2n}$/CB (n = 4, 5, 6)

Fig. 6a shows the results of linear sweep voltammetry (LSV) for each Ni catalyst [$Ni_n(PET)_{2n}$/CB (n = 4, 5, 6) and NiO-IM/CB] in 0.1 M potassium hydroxide (KOH). As we applied the potential from the negative side to the positive side, each Ni catalyst produced a larger oxidation current than CB without a Ni catalyst. It can be understood that among the observed oxidation currents, the peak at 1.35 V *vs.* the reversible hydrogen electrode

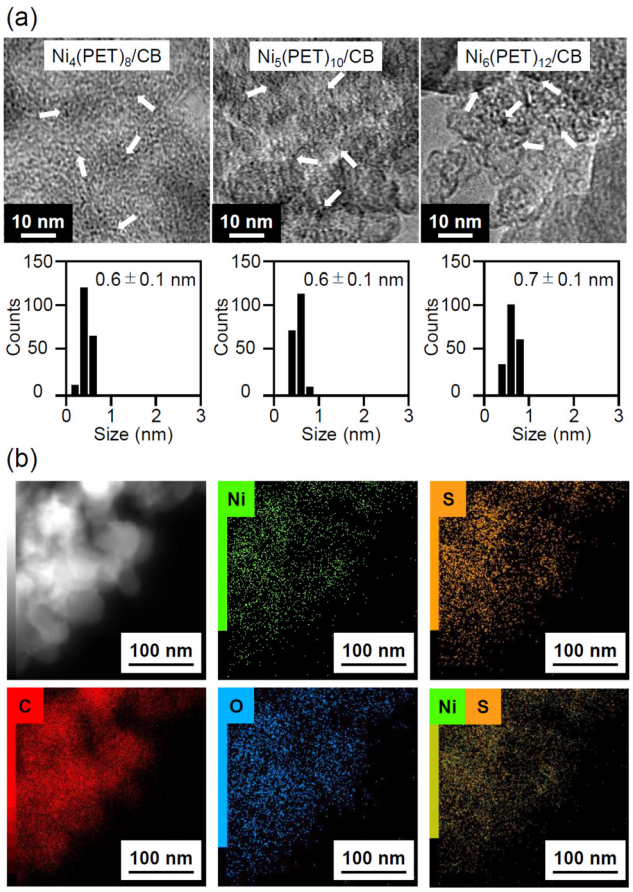

Fig. 5 (a) TEM images and the resulting histograms of particle-size distribution of $Ni_4(PET)_8$/CB (left), $Ni_5(PET)_{10}$/CB (middle) and $Ni_6(PET)_{12}$/CB (right). (b) HAADF-STEM images and EDS elemental mapping (Ni, S, C and O) of $Ni_5(PET)_{10}$/CB. In (a) and (b), the loading weights of Ni are 0.5 and 5 wt%, respectively.

(RHE) is attributed to the oxidation current derived from the change from Ni^{2+} to Ni^{3+}.[58] When we applied a more positive potential than 1.45 V *vs.* RHE, the current density caused by the OER increased dramatically. We defined the overpotential to be the applied potential until the current density reaches 10 mA cm^{-2} and show the overpotential in Table S7† for each Ni catalyst. These results reveal a 31 mV decrease in the overpotential of $Ni_5(PET)_{10}$/CB compared with NiO-IM/CB. Fig. 6b shows the OER mass activity per Ni weight (at 1.55 V *vs.* RHE) for each Ni catalyst [$Ni_n(PET)_{2n}$/CB (n = 4, 5, 6) and NiO-IM/CB]. Surprisingly, $Ni_5(PET)_{10}$/CB exhibited *ca.* 2.3 times higher OER mass activity than NiO-IM/CB. $Ni_4(PET)_8$/CB and $Ni_6(PET)_{12}$/CB also exhibited a slightly higher OER mass activity than NiO-IM/CB.

To confirm that we correctly evaluated the OER activity in these measurements, we calculated the Tafel slope at 1.55 V *vs.* RHE, at which the OER mass activity was compared, for each Ni catalyst (Table S7 and Fig. S20†). In the OER, the first step (Step I) is the adsorption of OH_{ads} to the bare metal site (typical Tafel slope: 120 mV dec^{-1}). In Step II, OH_{ads} is oxidized to O_{ads} (typical Tafel slope: 60 mV dec^{-1}), and in the sub-

Open Access Article. Published on 07 February 2023. Downloaded on 4/30/2026 8:17:38 PM.
This article is licensed under a Creative Commons Attribution-NonCommercial 3.0 Unported Licence.

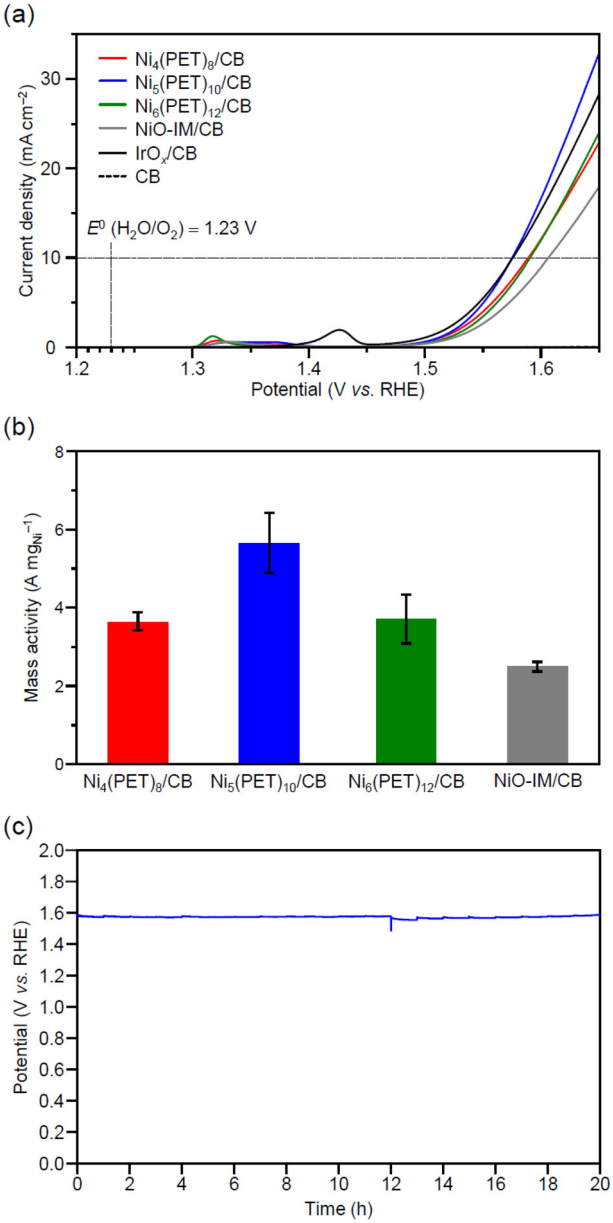

Fig. 6 (a) Linear sweep voltammetry (LSV) curves and (b) mass activity at 1.55 V *vs.* RHE for $Ni_n(PET)_{2n}$/CB (n = 4, 5, 6) and NiO-IM/CB on a glassy carbon (GC) electrode in 0.1 M KOH. (c) Chronopotentiometry curves for $Ni_5(PET)_{10}$/CB collected at 10 mA cm^{-2} for 20 hours on GC electrodes in 0.1 M KOH. The metal loading weight of all samples was 5 wt%, which was estimated by ICP-MS. In (a), LSV curves obtained for IrO_x/CB and CB are also shown for comparison.

sequent Step III, O_{ads} combines with a second OH^- to form OOH_{ads} (typical Tafel slope: 40 mV dec^{-1}). In the last Step IV, O_2 gas is released and bare metal sites are regenerated; these sites are again available for the catalytic cycle.[41,42] Considering this mechanism, if the obtained Tafel slope differed substantially from 40–120 mV dec^{-1}, the OER activity might not have been properly evaluated. In our measurements, the Tafel slope for $Ni_5(PET)_{10}$/CB near 1.55 V *vs.* RHE was 70 mV dec^{-1}, which confirms that we correctly evaluated the OER. Experiments with different loading weights of Ni catalysts confirmed that the OER activity can be correctly evaluated even at a lower loading weight of 0.5 wt% (Fig. S21†).

Regarding $Ni_5(PET)_{10}$/CB, which exhibited the highest activity, we also evaluated the durability of the activity (Fig. 6c, and S22†). Specifically, we performed chronopotentiometry at a current density of 10 mA cm^{-2} (1.96 mA). We observed no increase in the applied potential after 20 hours, and $Ni_5(PET)_{10}$/CB exhibited a stable OER activity. To investigate the change in the particle size of $Ni_5(PET)_{10}$/CB with the applied potential, we also obtained TEM images of $Ni_5(PET)_{10}$/CB after an applied potential (Fig. S16–S18†). The average particle size of $Ni_5(PET)_{10}$/CB after the applied potential was 0.6 ± 0.2 nm, which is similar to that of $Ni_5(PET)_{10}$/CB before the applied potential. These results indicate that the applied potential did not cause aggregation of $Ni_5(PET)_{10}$/CB (Fig. S16†).

Origin of high OER activity of $Ni_n(PET)_{2n}$/CB (n = 4, 5, 6)

To clarify the origin of the specifically high OER activity of $Ni_5(PET)_{10}$/CB, we performed XAFS measurements on $Ni_5(PET)_{10}$/CB after applied potentials. Fig. 7a shows the Ni K-edge XANES spectra of $Ni_5(PET)_{10}$/CB upon an applied potential from 1.2–1.5 V *vs.* RHE. The absorption intensity at ~8348 eV gradually increased as the applied potential shifted toward the positive side. When the applied potential increased

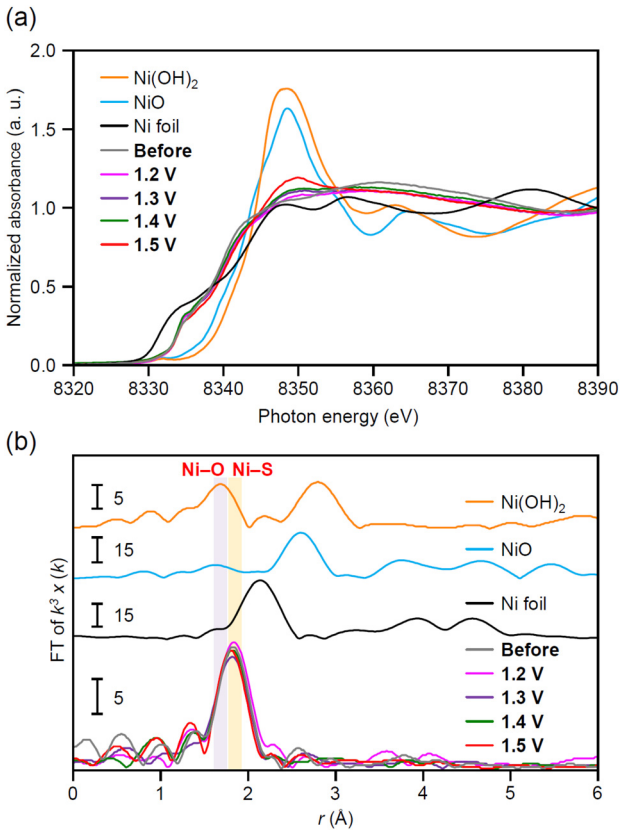

Fig. 7 Ni K-edge (a) XANES spectra and (b) FT-EXAFS spectra for $Ni_5(PET)_{10}$/CB before and after applied potential at 1.2–1.5 V *vs.* RHE. Ni foil, NiO and $Ni(OH)_2$ are also shown for comparison.

Open Access Article. Published on 07 February 2023. Downloaded on 4/30/2026 8:17:38 PM.
This article is licensed under a Creative Commons Attribution-NonCommercial 3.0 Unported Licence.

to 1.5 V *vs.* RHE, $Ni_5(PET)_{10}$/CB was substantially oxidized. Fig. 7b shows the Ni K-edge FT-EXAFS spectra of $Ni_5(PET)_{10}$/CB upon an applied potential from 1.2–1.5 V *vs.* RHE. The peak derived from the Ni–S bond (~1.9 Å) slightly shifted toward a short bond length after the applied potential. These results indicate that the Ni–O bond (~1.8 Å) was generated after the applied potential, demonstrating that an OER intermediate was formed. The obvious Ni–O bond was observed when the applied potential was increased up to 1.6 V *vs.* RHE. We also observed such a change in the electronic structure for $Ni_4(PET)_8$/CB and $Ni_6(PET)_{12}$/CB after the LSV measurements (Fig. S23†). However, the changes in the electronic structure of $Ni_4(PET)_8$/CB and $Ni_6(PET)_{12}$/CB before and after the LSV measurements were smaller than those of $Ni_5(PET)_{10}$/CB (Fig. S23†). These results indicate that the OER intermediates adsorbed with oxygen formed more easily in $Ni_5(PET)_{10}$/CB than in $Ni_4(PET)_8$/CB and $Ni_6(PET)_{12}$/CB upon the applied potential. Based on the geometric structure of $Ni_n(PET)_{2n}$ (n = 4, 5, 6) obtained by SC-XRD, the exposed area of the Ni sites (4–6 Å) in **2** was larger than those in **1** and **3**. Therefore, OH^- (2.67 Å) should more easily approach the Ni site in **2** than in **1** and **3** (Fig. 8 and S24†). This is probably the main reason why $Ni_5(PET)_{10}$/CB formed the OER intermediate more easily than $Ni_4(PET)_8$/CB and $Ni_6(PET)_{12}$/CB, and thereby the reaction proceeded more easily on $Ni_5(PET)_{10}$/CB than on $Ni_4(PET)_8$/CB and $Ni_6(PET)_{12}$/CB.

To investigate the reason why $Ni_5(PET)_{10}$/CB exhibited a higher OER activity than NiO-IM/CB, we also evaluated the change in the electronic structure of Ni before and after an applied potential to NiO-IM/CB (Fig. S25†). The electronic structure of NiO-IM/CB is almost the same before and after the applied potential. For NiO-IM/CB prepared by calcination, a phase change is unlikely to occur during the applied potential, different from the case of the active transition metal sulfides,[59] since a stable NiO phase is formed. We assumed that the dependence of the electronic structure of the Ni catalyst on the applied potential was one factor in the differences in the OER activities.

Finally, we note that the OER activity and electronic structure of the catalysts obtained in this study were substantially different from those of $Ni_n(PET)_{2n}$/CB in the previous report.[43] For example, the OER activity in this study was higher than that in the previous report and exhibited a different dependence on the number of metal atoms. In this study, we added Nafion during the catalyst slurry preparation. Thus, the interactions between $Ni_n(PET)_{2n}$ and the support, the accessibility of the substrate to the $Ni_n(PET)_{2n}$ surface, and the stability of the reaction intermediates should be different from those in the previous report. We assume that this difference in the catalyst slurry preparation resulted in the different OER activity and electronic structure during the reaction from those in the previous report.[43]

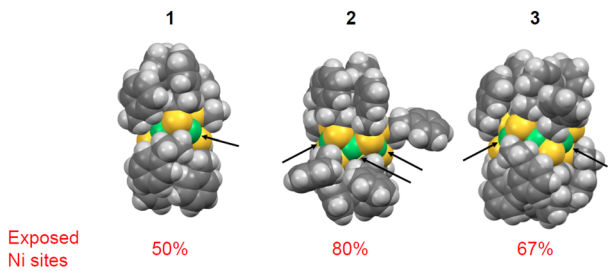

Fig. 8 Space-filling models and percentage of exposed Ni sites in $Ni_n(PET)_{2n}$ (n = 4, 5, 6). The arrows indicate exposed Ni sites. The ratio of exposed Ni sites was estimated by dividing the amount of Ni sites with the exposed area (4–6 Å) by all Ni sites.

Conclusions

We synthesized Ni TNCs protected by the same SR ligands {$[Ni_n(PET)_{2n}]^0$; n = 4, 5, 6} with atomic precision. For $Ni_5(PET)_{10}$, we succeeded in determining the geometric structure by SC-XRD for the first time; $[Ni_5(PET)_{10}]^0$ exhibited a distorted geometric structure and a larger exposed area of Ni sites than $[Ni_n(PET)_{2n}]^0$ (n = 4, 6). We have also succeeded in loading the obtained Ni TNCs on CB without aggregation. Interestingly, $Ni_5(PET)_{10}$/CB exhibited the highest OER activity among $[Ni_n(PET)_{2n}]^0$ (n = 4, 5, 6) thus prepared. It can be considered that the external reactants easily approach the Ni site of $Ni_5(PET)_{10}$ since the Ni site is largely exposed in $Ni_5(PET)_{10}$ than in $Ni_4(PET)_8$ and $Ni_6(PET)_{12}$. We expect that these findings lead to the elucidation of the mechanism of high OER activity of Ni sulfides and thereby the development of OER catalysts with a higher activity. In a future study, it is expected that the formation mechanism of the OER intermediates of $Ni_5(PET)_{10}$ will be elucidated by DFT calculations to provide a clear design guideline for synthesizing materials with activity exceeding that of conventional OER materials.

Experimental

Synthesis of $Ni_n(PET)_{2n}$ (n = 4, 5, 6)

$Ni_n(PET)_{2n}$ (n = 4, 5, 6) were synthesized using the reported method[49] by Z. Wang *et al.* with some modifications (Scheme S1†). The entire reaction was carried out in a 50 mL vial at 25 °C under air. First, nickel nitrate hexahydrate ($NiNO_3{\cdot}6H_2O$, 200 mg, 0.69 mmol) was added to *n*-propanol (12 mL) and stirred for 20 min until complete dissolution. The solution was then stirred vigorously and 2-phenylethanethiol (0.186 mL, 1.38 mmol) was slowly added to the solution. At this time, the color of the solution gradually changed from light green to brown. The solution was stirred for 15 min to facilitate the complete reaction of Ni^{2+} with 2-phenylethanethiol. Triethylamine (NEt_3, 0.5 mL) was then added rapidly to the solution and the color of the solution immediately changed to dark brown. After stirring for 3 h, the crude products were washed three times with methanol to remove unreacted precursors. The crude products were then extracted with dichloromethane (DCM) and were separated by TLC (DCM : hexane = 3 : 4, v : v). Layers **1–3** from the top of the TLC

 This journal is © The Royal Society of Chemistry 2023

Open Access Article. Published on 07 February 2023. Downloaded on 4/30/2026 8:17:38 PM.
This article is licensed under a Creative Commons Attribution-NonCommercial 3.0 Unported Licence.

shown in Fig. S26† were collected and extracted with DCM (**1–3**). Regarding **2**, the single crystal of **2** was obtained using a liquid–liquid diffusion method (DCM : methanol = 1 : 2) and its geometric structure was determined by SC-XRD (Table S2†).

Preparation of Ni catalyst

Loading of $Ni_n(PET)_{2n}$ (n = 4, 5, 6) on CB. First, 50 mg of CB was added to THF (30 mL) and sonicated for 20 min to disperse the CB in the solution. The THF solution containing dissolved **1–3** was added to THF-dispersed CB such that the Ni loading was 5 wt%. The amount of Ni loaded on CB was estimated by performing inductively coupled plasma mass spectrometry for the supernatant solution after adsorbing $Ni_n(PET)_{2n}$ on CB. Then, the THF mixture was volatilized by stirring at 60 °C for 30 min. Finally, the products were dried in a desiccator overnight to obtain $Ni_n(PET)_{2n}$/CB (n = 4, 5, 6) (Scheme S2†).

Preparation of Ni catalyst using the conventional IM method. NiO films obtained by calcination of Ni foil are often used as Ni catalysts for the general OER.[60] However, we prepared NiO-IM/CB using an impregnation method for comparison with $Ni_n(PET)_{2n}$/CB (n = 4, 5, 6) with the same support (CB). In the preparation of NiO-IM/CB, CB (50 mg) was first mixed with H_2O (15 mL) and 2-propanol (15 mL), and the solution was sonicated for 10 min to disperse the CB in the mixture (Scheme S3†). Nickel nitrate (loading: 5 wt%) was added to the mixture, which was stirred at 140 °C for 1 h, resulting in volatilization of the solvent. The product was dried in a desiccator and subsequently calcined at 200 °C for 20 min, resulting in the formation of NiO-IM/CB. XAFS and powder X-ray diffraction measurements (Fig. S25†) confirmed that the supported NPs were NiO NPs. TEM measurements (Fig. S16†) confirmed that the NiO-IM/CB has a particle size of 7.1 ± 1.4 nm.

Electrochemical measurements

The prepared Ni catalysts [$Ni_n(PET)_{2n}$/CB; n = 4, 5, 6, NiO-IM/CB] were added to a solution (12.8 mg for $Ni_n(PET)_{2n}$/CB and 10.6 mg for NiO-IM/CB) consisting of ultrapure water (19.1 mL), 2-propanol (6 mL), and Nafion solution (100 μL). The obtained mixture was sonicated in an ice-water bath for 30 min to disperse the Ni catalyst and afford a catalyst slurry. The catalyst slurry (10 μL) was cast spread over an entire glassy carbon (GC) electrode and dried at 60 °C for 15 min. Then, electrochemical measurements were performed in 0.1 M KOH using the GC coated with the prepared catalyst slurry as the working electrode, a Pt coil counter electrode, and a silver/silver chloride (Ag/AgCl) reference electrode to form a three-electrode system (Fig. S27†). The detailed protocol of the electrochemical measurements[61] is shown in Schemes S4 and S5.†

Author contributions

T. K. and Y. Negishi conceived the research and designed the experiments. T. K., S. H., Y. Niihori, and Y. Negishi designed the synthesis and electrocatalytic tests. S. F., T. O., and K. T. performed the synthesis, characterization, and electrocatalytic activity procedures. T. N., M. Takagi, T. S. and M. Tachikawa performed the theoretical calculations. T. K., S. K., and S. Y. performed the XAFS measurements. T. K. and Y. Negishi wrote the manuscript.

Conflicts of interest

There are no conflicts to declare.

Acknowledgements

We thank Yuki Iwamatsu (Tokyo University of Science) for technical assistance. This work was supported by the Japan Society for the Promotion of Science (JSPS) KAKENHI (grant number 20H02698 and 20H02552), the Scientific Research on Innovative Areas "Innovations for Light-Energy Conversion" (grant number 18H05178 and 20H05115), and the Scientific Research on Innovative Areas "Hydrogenomics" (grant number 21H00026 and 21H00027). Funding from the Yazaki Memorial Foundation for Science and Technology, the Sasakawa Scientific Research Grant from the Japan Science Society, the Advanced Technology Institute Research Grants 2022, and a TEPCO Memorial Foundation Research Grant (Basic Research) is gratefully acknowledged.

References

1 I. Chakraborty and T. Pradeep, *Chem. Rev.*, 2017, **117**, 8208–8271.
2 N. A. Sakthivel and A. Dass, *Acc. Chem. Res.*, 2018, **51**, 1774–1783.
3 M. Agrachev, M. Ruzzi, A. Venzo and F. Maran, *Acc. Chem. Res.*, 2019, **52**, 44–52.
4 B. Nieto-Ortega and T. Bürgi, *Acc. Chem. Res.*, 2018, **51**, 2811–2819.
5 Z. Gan, N. Xia and Z. Wu, *Acc. Chem. Res.*, 2018, **51**, 2774–2783.
6 Q. Yao, T. Chen, X. Yuan and J. Xie, *Acc. Chem. Res.*, 2018, **51**, 1338–1348.
7 T. Tsukuda and H. Häkkinen, *Protected Metal Clusters: From Fundamentals to Applications*, Elsevier, Amsterdam, 2015.
8 J. Yan, B. K. Teo and N. Zheng, *Acc. Chem. Res.*, 2018, **51**, 3084–3093.
9 T. Kawawaki, A. Ebina, Y. Hosokawa, S. Ozaki, D. Suzuki, S. Hossain and Y. Negishi, *Small*, 2021, **17**, 2005328.
10 T. Kawawaki, Y. Negishi and H. Kawasaki, *Nanoscale Adv.*, 2020, **2**, 17–36.
11 T. Kawawaki, Y. Mori, K. Wakamatsu, S. Ozaki, M. Kawachi, S. Hossain and Y. Negishi, *J. Mater. Chem. A*, 2020, **8**, 16081–16113.

Open Access Article. Published on 07 February 2023. Downloaded on 4/30/2026 8:17:38 PM.
This article is licensed under a Creative Commons Attribution-NonCommercial 3.0 Unported Licence.

12 T. Kawawaki, Y. Kataoka, M. Hirata, Y. Akinaga, R. Takahata, K. Wakamatsu, Y. Fujiki, M. Kataoka, S. Kikkawa, A. S. Alotabi, S. Hossain, D. J. Osborn, T. Teranishi, G. G. Andersson, G. F. Metha, S. Yamazoe and Y. Negishi, *Angew. Chem., Int. Ed.*, 2021, **60**, 21340–21350.
13 T. Kawawaki, Y. Kataoka, M. Hirata, Y. Iwamatsu, S. Hossain and Y. Negishi, *Nanoscale Horiz.*, 2021, **6**, 409–448.
14 X. Gao and W. Chen, *Chem. Commun.*, 2017, **53**, 9733–9736.
15 J. Chen, L. Liu, X. Liu, L. Liao, S. Zhuang, S. Zhou, J. Yang and Z. Wu, *Chem. – Eur. J.*, 2017, **23**, 18187–18192.
16 T. Imaoka, Y. Akanuma, N. Haruta, S. Tsuchiya, K. Ishihara, T. Okayasu, W.-J. Chun, M. Takahashi and K. Yamamoto, *Nat. Commun.*, 2017, **8**, 688.
17 J. Chen, Y. Pan, Z. Wang and P. Zhao, *Dalton Trans.*, 2017, **46**, 12964–12970.
18 J. Chen, L. Liu, L. Weng, Y. Lin, L. Liao, C. Wang, J. Yang and Z. Wu, *Sci. Rep.*, 2015, **5**, 16628.
19 C. Zhang, T. Matsumoto, M. Samoc, S. Petrie, S. Meng, T. C. Corkery, R. Stranger, J. Zhang, M. G. Humphrey and K. Tatsumi, *Angew. Chem., Int. Ed.*, 2010, **49**, 4209–4212.
20 P. Woodward, L. F. Dahl, E. W. Abel and B. C. Crosse, *J. Am. Chem. Soc.*, 1965, **87**, 5251–5253.
21 E. W. Abel and B. C. Crosse, *J. Chem. Soc. A*, 1966, 1377–1378.
22 R. O. Gould and M. M. Harding, *J. Chem. Soc. A*, 1970, 875–881.
23 H. Barrera, J. C. Bayón, J. Suades, C. Germain and J. P. Declerq, *Polyhedron*, 1984, **3**, 969–975.
24 I. G. Dance, M. L. Scudder and R. Secomb, *Inorg. Chem.*, 1985, **24**, 1201–1208.
25 M. Kriege and G. Henkel, *Z. Naturforsch., B: Chem. Sci.*, 1987, **42**, 1121–1128.
26 B.-K. Koo, E. Block, H. Kang, S. Liu and J. Zubieta, *Polyhedron*, 1988, **7**, 1397–1399.
27 T. Krüger, B. Krebs and G. Henkel, *Angew. Chem., Int. Ed. Engl.*, 1989, **28**, 61–62.
28 T. Krüger, B. Krebs and G. Henkel, *Angew. Chem., Int. Ed. Engl.*, 1992, **31**, 54–56.
29 A. H. Mahmoudkhani and V. Langer, *Inorg. Chim. Acta*, 1999, **294**, 83–86.
30 A. H. Mahmoudkhani and V. Langer, *Polyhedron*, 1999, **18**, 3407–3410.
31 S. A. Ivanov, M. A. Kozee, W. A. Merrill, S. Agarwal and L. F. Dahl, *J. Chem. Soc., Dalton Trans.*, 2002, 4105–4115.
32 C. Zhang, S. Takada, M. Kölzer, T. Matsumoto and K. Tatsumi, *Angew. Chem., Int. Ed.*, 2006, **45**, 3768–3772.
33 R. Angamuthu, H. Kooijman, M. Lutz, A. L. Spek and E. Bouwman, *Dalton Trans.*, 2007, 4641–4643.
34 C. Tan, M. Jin, X. Ma, Q. Zhu, Y. Huang, Y. Wang, S. Hu, T. Sheng and X. Wu, *Dalton Trans.*, 2012, **41**, 8472–8476.
35 M. Zhu, S. Zhou, C. Yao, L. Liao and Z. Wu, *Nanoscale*, 2014, **6**, 14195–14199.
36 X. Chai, T. Li, M. Chen, R. Jin, W. Ding and Y. Zhu, *Nanoscale*, 2018, **10**, 19375–19382.
37 Z. Zhuang and W. Chen, *Analyst*, 2020, **145**, 2621–2630.
38 H. N. Kagalwala, E. Gottlieb, G. Li, T. Li, R. Jin and S. Bernhard, *Inorg. Chem.*, 2013, **52**, 9094–9101.
39 R. Angamuthu and E. Bouwman, *Phys. Chem. Chem. Phys.*, 2009, **11**, 5578–5583.
40 W. Hu, Y. Sun, S. Li, X. Cheng, X. Cai, M. Chen and Y. Zhu, *CCS Chem.*, 2021, **3**, 2509–2519.
41 D. R. Kauffman, D. Alfonso, D. N. Tafen, J. Lekse, C. Wang, X. Deng, J. Lee, H. Jang, J.-s. Lee, S. Kumar and C. Matranga, *ACS Catal.*, 2016, **6**, 1225–1234.
42 K. S. Joya, L. Sinatra, L. G. AbdulHalim, C. P. Joshi, M. N. Hedhili, O. M. Bakr and I. Hussain, *Nanoscale*, 2016, **8**, 9695–9703.
43 S. Srinivasan, Z. Liu, S. House and R. Jin, *Inorg. Chem.*, 2023, **62**, 1875–1884.
44 K. Kwak and D. Lee, *Acc. Chem. Res.*, 2019, **52**, 12–22.
45 M. H. Naveen, R. Khan and J. H. Bang, *Chem. Mater.*, 2021, **33**, 7595–7612.
46 Y. Du, H. Sheng, D. Astruc and M. Zhu, *Chem. Rev.*, 2020, **120**, 526–622.
47 T. Kawawaki and Y. Negishi, *Nanomaterials*, 2020, **10**, 238.
48 B. Kumar, T. Kawawaki, N. Shimizu, Y. Imai, D. Suzuki, S. Hossain, L. V. Nair and Y. Negishi, *Nanoscale*, 2020, **12**, 9969–9979.
49 Y. Pan, J. Chen, S. Gong and Z. Wang, *Dalton Trans.*, 2018, **47**, 11097–11103.
50 D. Y. Chung, J. W. Han, D.-H. Lim, J.-H. Jo, S. J. Yoo, H. Lee and Y.-E. Sung, *Nanoscale*, 2015, **7**, 5157–5163.
51 Q. Li, D. Wang, C. Han, X. Ma, Q. Lu, Z. Xing and X. Yang, *J. Mater. Chem. A*, 2018, **6**, 8233–8237.
52 Y. Hattori, T. Konishi and K. Kaneko, *Chem. Phys. Lett.*, 2002, **355**, 37–42.
53 Q. Ma, C. Hu, K. Liu, S.-F. Hung, D. Ou, H. M. Chen, G. Fu and N. Zheng, *Nano Energy*, 2017, **41**, 148–153.
54 M. A. Peck and M. A. Langell, *Chem. Mater.*, 2012, **24**, 4483–4490.
55 G. Zhao, P. Li, N. Cheng, S. X. Dou and W. Sun, *Adv. Mater.*, 2020, **32**, 2000872.
56 P. Alemany and R. Hoffmann, *J. Am. Chem. Soc.*, 1993, **115**, 8290–8297.
57 S. Hossain, Y. Imai, Y. Motohashi, Z. Chen, D. Suzuki, T. Suzuki, Y. Kataoka, M. Hirata, T. Ono, W. Kurashige, T. Kawawaki, T. Yamamoto and Y. Negishi, *Mater. Horiz.*, 2020, **7**, 796–803.
58 Y. Dou, L. Zhang, J. Xu, C.-T. He, X. Xu, Z. Sun, T. Liao, B. Nagy, P. Liu and S. X. Dou, *ACS Nano*, 2018, **12**, 1878–1886.
59 M. Wang, Q. Wa, X. Bai, Z. He, W. S. Samarakoon, Q. Ma, Y. Du, Y. Chen, H. Zhou, Y. Liu, X. Wang and Z. Feng, *JACS Au*, 2021, **1**, 2216.
60 P. T. Babar, A. C. Lokhande, M. G. Gang, B. S. Pawar, S. M. Pawar and J. H. Kim, *J. Ind. Eng. Chem.*, 2018, **60**, 493–497.
61 C. Wei, R. R. Rao, J. Peng, B. Huang, I. E. L. Stephens, M. Risch, Z. J. Xu and Y. Shao-Horn, *Adv. Mater.*, 2019, **31**, 1806296.

 This journal is © The Royal Society of Chemistry 2023